ANALYSIS OF PULSE TO PULSE AMPLITUDE AND PHASE VARIATIONS FOR DIFFERENT LEO OBJECTS USING S3TSR RADAR MEASUREMENTS

Rafael Casado[(1)], Jacobo Martínez-Villa[(1)], Marco Alessandrini[(2)], Pier Mario Besso[(2)], Cristina Pérez[(3)], Igone Urdampilleta[(4)]

[(1)]Indra Sistemas, Crta Loeches 9, 28850 Torrejón de Ardoz, Madrid, Spain.
Email: {rcasado, jmartinezv} @indra.es
[(2)] ESA/ESOC, Robert-Bosch-Str. 5, 64293 Darmstadt, Germany,
Email: {marco.alessandrini, pier.mario.besso} @esa.int
[(3)] CDTI, Cid 4, Madrid, Spain. Email: cristina.perez@cdti.es
[(4)] Email: sst.spain@cdti.es

1 ABSTRACT

The space objects in LEO regime present high velocities and accelerations due to the low altitude. This article analyses several passes of different objects across the Field of Regard (FoR) of a surveillance radar, the S3TSR. The S3TSR (Spanish Space Surveillance and Tracking - Surveillance Radar) is a surveillance radar system developed by Indra within a project funded by the Spanish Administration through CDTI and technically managed by ESA.

This radar contributes providing daily measurements to the EUSST Partnership. It is being maintained successfully and operated 24/7 since January 2019 by the COVE (Centro de Operaciones de Vigilancia Espacial / Space Surveillance Operation Centre) from the Spanish Air and Space Force.

This study is beneficial to having a deeper knowledge on correlation between estimated variation of RCS and complexity of the object. The analysis consists of three phases. First, the acquisition of amplitude and phase measurements in consecutive pulses, bounced in LEO objects with different shape complexity. Second, the removal of the contribution of variables already known and third, the comparison of these refined data with the theoretical model.

2 INTRODUCTION

The S3TSR is a close-monostatic ground-based pulsed radar system consisting of one transmitting antenna and one receiving antenna, both pure phased arrays, operating at L band.

The S3TSR uses a scalable architecture, being therefore upgradeable in later stages of the radar life.

It is capable of providing positional information of orbital objects by means of space surveillance.

The transmitting subsystem is based on a distributed transmitter architecture, composed of a number of identical solid-state modules.

The receiving subsystem is based on a single replicated active module that performs reception and beamforming.

The Rx and Tx Antennas are composed of identical building blocks (sub-arrays) attached to a supporting structure.

The S3TSR is currently operating nominally using a surveillance operational mode. This operational mode explores the complete FoR volume in less than 8s.

Since the surveillance mode does not receive any a priori information about objects, the beam sequence that is used is a fixed pattern repeated periodically (a beam sequence is a series of pencil beams pointing to a certain angle U/V).

This fixed scanning pattern generates detections (called plots). Each plot contains time, angle, range, range rate, RCS and SNR information.

These plots are correlated to find coincidences in time, range and angles in order to determine if they can be assigned to objects to form tracks (a track is merely defined as a collection of plots).

The information provided by the radar in the individual plots has been found coherent so far. However, it results desirable to analyse in detail the amplitude and phase of the individual pulses and detections in order to enable potential improvements.

Thus, the purpose of this study is to analyze some selected objects crossing the FoR of the radar, each of one with different shape, studying closely the amplitude and phase of the signal backscattered by each object.

To this end, it was developed and tested an experimental software that would, at a given moment, execute a beam sequence, in which the TX beams applied would match the predicted angular position during a pass across the

FoR of the preselected object.

Because the S3TSR radar is being permanently operated, a scheduled stop of the system was requested and granted.

This experiment took place on 22nd of December 2022.

3 AN EXPERIMENTAL OPERATIONAL MODE

The experimental software works as follows: It programs the mentioned special beam sequence in the radar. Some moments before the object enters inside the FoR, the radar changes its normal operational mode to the experimental beam sequence, following the preselected object during the whole pass. When finished executing that special beam sequence, the normal operation resumes.

This beam sequence is the same as the nominal sequence, but having a different number of beams (and, therefore, different scan duration) and with U/V pointing of the beams that coincide with the angular coordinates that the tracked object is having in the selected pass, according to the predicted trajectory.

The Tx antenna beamwidth of the S3TSR Down Scale implementation is much wider than in the Rx antenna. The normal operational mode uses many Rx beams to cover the Tx beamwidth but for this specific application the approach is different, as only the four central Rx beams will receive echoes from the target.

Therefore, in this experiment only the four central Rx beams were processed.

Besides the mentioned changes in the scanning, an already implemented mechanism for extracting raw data from the radar during the pass was used. This raw data flow is required in order to post-process adequately the pulses.

Regarding operation, a window is presented enabling the user to select a file containing the orbital parameters of the objects' list considered candidates for tracking in TLE format.

The file should have been downloaded not long before the instant in which the test is to be carried out, so that the parameters are sufficiently valid and the predicted trajectory from them adjusts to the real one.

After selecting the file, the experimental software propagates the trajectories of all objects in the list during the specified interval using an SGP4 propagator.

Then, the experimental software calculates passes of objects crossing the FoR of the radar. The resulting information is presented to the user in a list as depicted in the following figure:

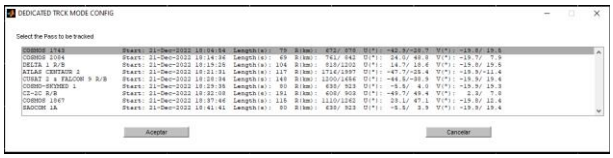

Figure 1. Selection of object

This list provides the name of the object, start instant, pass duration, minimum and maximum range during the pass and U/V coordinate ranges.

Once a valid pass is selected, the experimental software calculates the number of beams and pointing angles required for the pass and synthesizes the beam sequence.

Finally, it waits for the right moment to command the reconfiguration to the synthesis unit and signal processors and synchronously commands a change of operational mode.

4 LIST OF OBJECTS

The following table is the list of the 8 objects finally used for the study.

The information on size, shape and estimated radar section has been obtained from the ESA DISCOS database (https://discosweb.esoc.esa.int).

Some of the objects were selected randomly from the Celestrak selection of brightest objects. Some others were selected attending to its round/spherical shape. They are all public and known objects.

Table 1. Information extracted from DISCOS Database for selected objects.

Pass	Norad Id	Name	Object Class	Size meters (Depth/Height/Diam)	Shape/Mass(kg)	RCS (m²) Avg/Max/Min	Start/length (s)
1	20666	SL-6 R/B(2)	Rocket Body	3.3/3.3/2.3	Cyl/892	8/8.6/4.15	12:22:13 / 85
2	15483	SL-8 R/B	Rocket Body	6.57/6.57/2.4	Cyl/1421	14.6/16.4/4.5	12:41:14 / 135
3	25400	SL-16 R/B	Rocket Body	10.4/10.4/3.9	Cyl/8226	37.8/42.3/11.9	12:56:28 / 119
4	23087	COSMOS 2278	Payload	19/--/--	--/3221	--/133/38.5	13:07:04 / 128
5	22286	COSMOS 2228	Payload	13.1/3.2/1.3	Cyl+1Ant/1982	13.2/16.7/6	13:15:03/ 97
6	39267	DANDE	Payload	0.46/0.46/0.46	Sphere/46	0.196/0.196/0.196	13:31:29/ 65
7	00733	THOR AGENA D R/B	Rocket Body	6.3/6.3/1.5	Cyl+Nozzle/600	8.3/9.6/1.8	13:39:30/ 106
8	24298	SL-16 R/B	Rocket Body	10.4/10.4/3.9	Cyl/8226	37.8/42.3/11.9	13:58:22 / 135

5 DETECTABILITY AND ACCURACY ANALYSIS

Although the objective of the study is to analyze amplitudes and phases, it is interesting to begin the analysis of the collected detection data by counting the detections and reproducing the plot formation process.

Specifically, this analysis consists of:

- A filtering process applied in time and distance that allows selecting the detections that have been caused by the object, in each pass. In this process, only detections from Rx beam 1, 2, 3 and 4 are considered.

- Corrections are added to the coordinates of the detections that were not applied in the process phase in which the monitoring is carried out (but they are applied for the generation of the raw plots that are sent to the Data Processor).

- The process of forming elaborated plots that is carried out in the Data Processor is reproduced. When for each Tx beam there are several detections due to different Rx beams, a single plot is formed with all of them. Coordinates of this single plot are obtained by averaging those of the detections that have been merged into it.

- Additionally, corrections are applied to the distance coordinate of the plots to compensate for the Distance/Doppler coupling effect of the Linear Frequency Modulation (LFM).

The following table provides information about the detections and plots resulting from this analysis.

In general, beam 4 gives a higher percentage of detections, and the same happens with beam 3 in passes 1, 3 and 8. In the other passes, beam 1 is the second best, or even in some cases, it is the one producing most detections.

Regarding the plot count, under the column titled *Expected* the expected number of plots is presented, which match the number of Tx beams that have been arranged pointing at the object during the entire pass.

Under the column titled *Detected* there is the plot number arisen from processing the detections collected, together with the percentage that it represents with respect to the expected number. This percentage can be interpreted as average detection probability (Pd).

Table 2. Detections and resulting plots.

Pass #	NoradId	Name	Length	# Rx Beam Detections				# Plots	
			(s)	B #1	B #2	B #3	B #4	Expected	Detected
1	20666	SL-6 R/B(2)	85	565	556	629	643	643	649 (87.6 %)
2	15483	SL-8 R/B	135	358	239	177	350	350	393 (33.4 %)
3	25400	SL-16 R/B	119	456	446	635	699	699	712 (68.7 %)
4	23087	COSMOS 2278	128	546	388	342	537	537	587 (52.6 %)
5	22286	COSMOS 2228	97	515	312	253	525	526	557 (65.9 %)
6	39267	DANDE	65	47	3	3	50	60	95 (16.8 %)
7	00733	AGENA D R/B	106	644	495	539	698	698	705 (76.3 %)
8	24298	SL-16 R/B	135	926	891	1077	1108	1108	1114 (94.7 %)

As shown in the table, the average Pd is relatively low for some objects.

To analyse this question, losses relative to the reference situation applicable to the current version of the S3TSR are calculated below.

Said situation is summarized in the values obtained in the radar equation.

Specifically, the following figure offers a curve for each pass that represents versus time, the losses with respect to the reference situation. These losses are obtained by adding the following terms:

- Term associated with the distance, calculated as $40 \cdot \log_{10} \frac{R}{710.4}$, where R is the radar range to the target in km, according to the propagated trajectory.

- Rx beamshape loss term. At each detection opportunity, the smallest of the four values associated with the four Rx beams is considered.

- Term of theoretical losses due to deflection in Tx.

- Term of theoretical losses due to deflection in Rx.

Note that beam shape losses in Tx are not considered since they have been found to be negligible.

The change in atmospheric losses with respect to those considered in the calculation of the reference situation that corresponds to R = 710.4 km would also be insignificant.

The small variation in antenna gain due to operating at a frequency slightly lower than 1400 MHz (the one considered in the reference calculation) is also neglected.

It also happened that there were 4 out of 96 Tx antenna elements in failure condition, that is, they did not transmitted power during the test. This small reduction in transmitted power and antenna gain was neither taken into account in the loss calculation.

The obtained values are, in general, positive in losses, that is, the measurement is in worse conditions than in the reference situation.

Let's see these values case by case:

- For Pass #1 losses vary between 2.8 and 5.4 dB, which would be compensated with RCS between 1.9 and 3.5 m2. According to the ESA DISCOS database, the minimum RCS of the object is 4.15 m2, so it would be consistent with achieving a relatively high Pd (87.6%).

- For Pass #2 losses vary between 11 and 18.7 dB, which would be compensated with RCS between 12.5 and 75 m2. According to the ESA DISCOS database, the minimum RCS of the object is 4.5 m2, the average is 14.6 and the maximum is 16.4. It is coherent that the average Pd recorded is relatively poor (33.4%).

- For Pass #3 losses vary between 8.2 and 15 dB, which would be compensated with RCS between 6.6 and 31.3 m2. According to the ESA DISCOS database, the minimum RCS of the object is 11.9 m2, the average is 37.8 and the maximum is 42.3. In this case, a mean Pd greater than that obtained (68.7%) would have been expected.

- For Pass #4 the losses vary between 12.5 and 14.5 dB, which would be compensated with RCS between 18 and 28.3 m2. According to the ESA DISCOS database, the minimum RCS of the object is 38.5 m2 and the maximum is 133. In this case, an average Pd higher than that achieved (52.6%) would also have been expected.

- For Pass #5 the losses vary between 8.3 and 13.6 dB, which would be compensated with RCS between 6.8 and 22.9 m2. According to the ESA DISCOS database, the minimum RCS of the object is 6 m2, the average is 13.2 and the maximum is 16.7. The average Pd achieved (65.9%) would be more or less justifiable.

- For Pass #6 the losses vary between -0.15 and 2.2 dB, which would be compensated with RCS between 0.97 and 1.67 m2. According to the ESA DISCOS database, the RCS of the object is 0.196 m2, and it is a spherical object. It is totally justifiable that the object has hardly been detected (16.8% of average Pd) since the RCS is between 6.85 and 9.2 dB below what is necessary to compensate for the losses.

- For Pass #7 the losses vary between 7.3 and 10.6 dB, which would be compensated with RCS between 5.3 and 11.5 m2. According to the ESA DISCOS database, the minimum RCS of the object is 1.8 m2, the average is 8.3 and the maximum is 9.6. The average Pd achieved (76.3%) would be more or less justifiable.

- For Pass #8 the losses vary between 8.5 and 15.7 dB, which would be compensated with RCS between 7 and 37.7 m2. According to the ESA DISCOS database, the minimum RCS of the object is 11.9 m2, the average is 37.8 and the maximum is 42.3. It is consistent with achieving a relatively high mean Pd (94.7%).

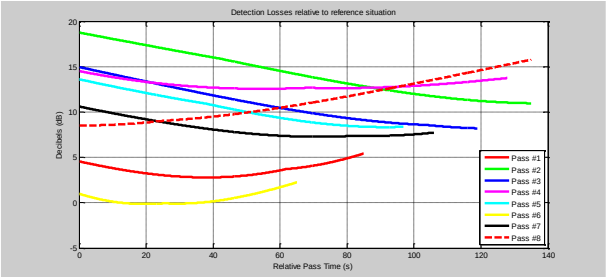

Figure 2. Detection losses relative to the reference situation (ideal radiation pattern).

The following figure again shows the global losses with respect to the reference situation, but calculating in this case the deflection losses from the diagram measurements of the element.

In the case of the Tx Antenna, it has been considered that the element radiation pattern of said antenna coincides with that of the Rx, something that is known not to be true, but may be more realistic than continuing to consider the simple model described above.

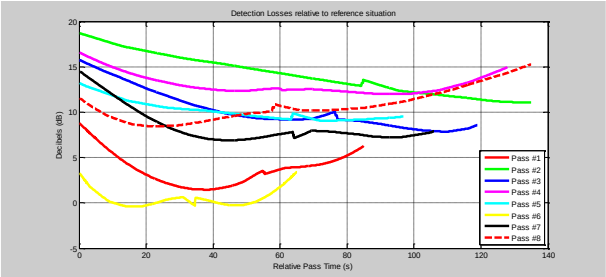

Figure 3. Detection losses relative to the reference situation (more realistic radiation pattern).

It can be seen that, although the values of both previous pictures are roughly similar, there are significant differences, and it usually happens in all passes that the maximum losses are greater with this second method of estimating deflection losses.

Regarding the angular accuracy, the following two figures show the U/V coordinates of "elaborated" plots that would be obtained after correlating the detections.

Points with a different colour for each pass represents each plot. Lines of the same colour represent the evolution of these same coordinates according to the estimated trajectory from the propagation of the TLE parameters (using SGP4).

In both cases, the coordinates are "geometric" and refer to the nominal orientation of the Rx antenna.

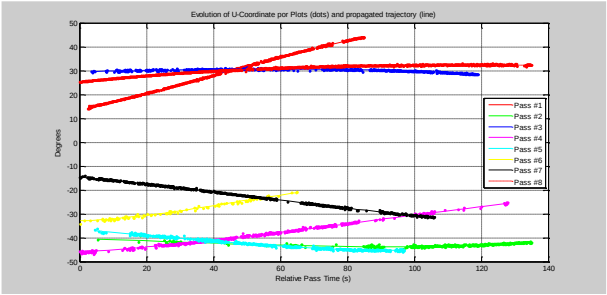

Figure 4. U-coordinate evolution vs time (dots are measurements, solid line are propagated TLEs).

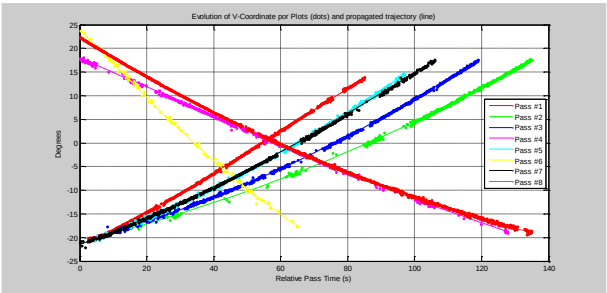

Figure 5. V-coordinate evolution vs time (dots are measurements, solid lines are propagated TLEs).

In these previous curves, it is possible to see regions in U/V where each object passes and the scattering of the dots with respect to the solid lines gives an idea of the angular accuracy.

It is also possible to see regions with less concentration of plots, in which detectability is reduced. This effect will be better observed when analyzing the amplitudes of the detections.

Following two curves directly show angular errors, calculated as the difference between the plot coordinate (U or V), and the estimated position coordinate of the object at the instant of the plot, according to SGP4 propagation.

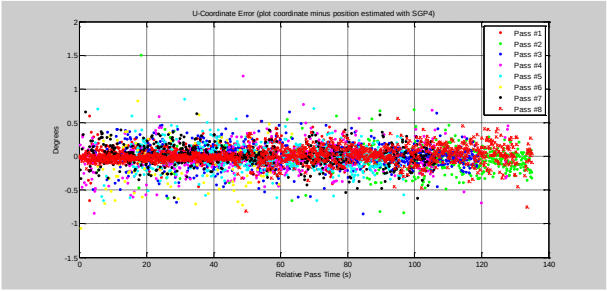

Figure 6. U-coordinate error

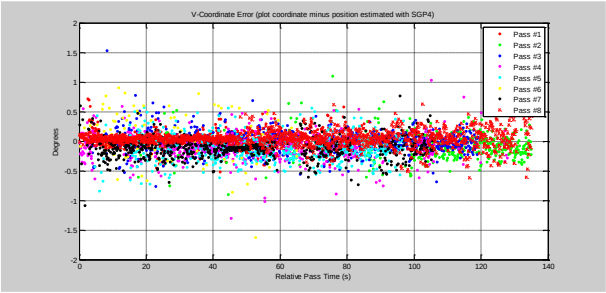

Figure 7. V-coordinate error

The following table offers a summary of the statistics of these errors for the 8 passes and for the total number of plots:

Table 3. Error statistics.

Pass #	NoradId	Name	# Plots	U - Coordinate		V - Coordinate	
				Mean (°)	Sigma (°)	Mean (°)	gma (°)
1	20666	SL-6 R/B(2)	649	0.041	0.121	0.035	0.137
2	15483	SL-8 R/B	393	-0.049	0.213	-0.083	0.225
3	25400	SL-16 R/B	712	0.006	0.174	-0.012	0.187
4	23087	COSMOS 2278	587	-0.023	0.193	-0.109	0.208
5	22286	COSMOS 2228	557	-0.019	0.186	-0.109	0.212
6	39267	DANDE	95	-0.130	0.329	0.070	0.425
7	00733	THOR AGENA D R/B	705	0.010	0.157	-0.115	0.173
8	24298	SL-16 R/B	1114	0.015	0.123	0.051	0.136
Total	--	--	4812	-0.000	0.170	-0.033	0.199

As it can be seen, both, in the previous table and figures, there is no clear repetition of average errors in several passes that could indicate that there is an offset in either of the two coordinates.

The obtained average errors could be a consequence of inaccuracies in the estimation of the orbit positions with SGP4 or inaccuracies in the earth orientation parameters (EOP).

It is also seen in the figures that there are cases with significantly high errors. Out of curiosity, the following table presents the statistics again, but applying a filter that removes 2% of outlayers:

Table 4. Error statistics (without outlayers).

Pass #	NoradId	Name	# Plots	U - Coordinate		V - Coordinate	
				Mean (°)	Sigma (°)	Mean (°)	gma (°)
1	20666	SL-6 R/B(2)	636	0.044	0.103	0.034	0.117
2	15483	SL-8 R/B	385	-0.055	0.176	-0.092	0.197
3	25400	SL-16 R/B	698	0.010	0.154	-0.017	0.159
4	23087	COSMOS 2278	575	-0.024	0.166	-0.110	0.174
5	22286	COSMOS 2228	546	-0.019	0.164	-0.115	0.194

6	39267	DANDE	93	-0.130	0.302	0.098	0.379
7	00733	THOR AGENA D R/B	691	0.010	0.140	-0.118	0.152
8	24298	SL-16 R/B	1092	0.013	0.105	0.056	0.117
Total	--	--	4716	-0.000	0.149	-0.035	0.178

Regarding the range coordinate, the following picture shows the evolution of both, dots (measurement) and the estimated position of the object (solid line of the same color).

It refers in both curves to geometric distance. The correction required to compensate for the Distance/Doppler coupling of the LFM has already been applied.

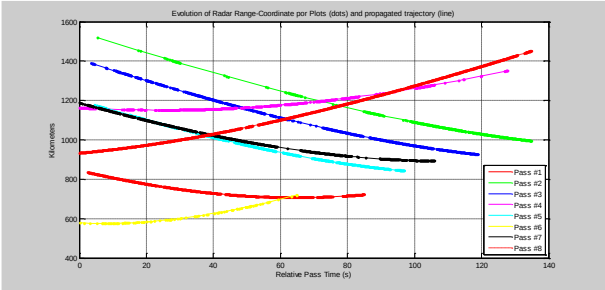

Figure 8. Range evolution vs time (dots are measurements, solid lines are propagated TLEs).

The following figure already provides the distance error, defined as the difference between the distance estimated for the plot, and the distance calculated from the propagated orbit. These error values are already provided directly in meters.

In this case, it is perfectly clear that the evolution of the average error is due to the imprecision in the estimation of the orbit from the SGP4 propagator and the considered TLE parameters.

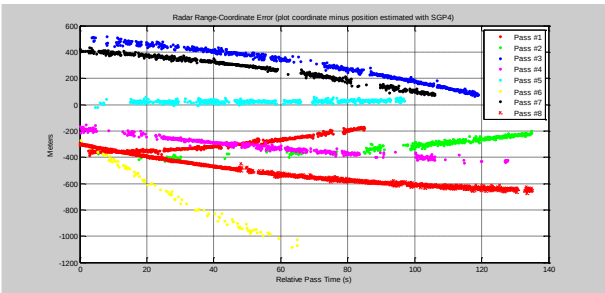

Figure 9. Range error evolution vs time.

If the evolution of the average error is estimated (by means of an order 3 polynomial adjusted by Least Mean Square (LMS)) and said average error is subtracted from errors associated with the plots, then the following figure is obtained:

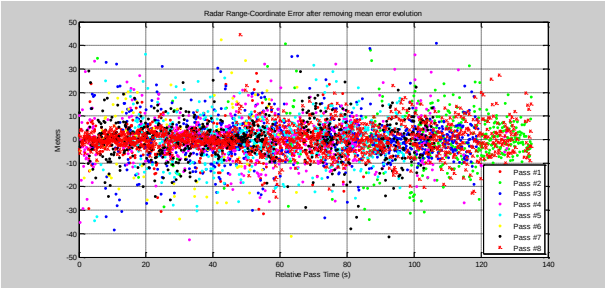

Figure 10. Range error evolution vs time after removing mean error.

The following table shows sigma values derived from the values of the previous picture.

Table 5. Sigma range (after removing mean error).

Pass #	NoradId	Name	Sigma Range (m)
1	20666	SL-6 R/B(2)	6.7
2	15483	SL-8 R/B	11.3
3	25400	SL-16 R/B	9.7
4	23087	COSMOS 2278	9.4
5	22286	COSMOS 2228	9.3
6	39267	DANDE	16.0
7	00733	THOR AGENA D R/B	8.2
8	24298	SL-16 R/B	6.4
Total	--	--	8.7

6 ANALYSIS OF SIGNAL AMPLITUDES

In this section, the signal amplitude of the collected detections is represented. Specifically the sum channel signal levels of the Rx detection beams that, at each moment, provide a greater S/N ratio.

In general, the beam detection is considered the one that, at each moment, has the smallest losses due to beamshape, which is in most cases the #4 beam, in others the #1 beam or the #3 beam.

In the next eight figures amplitudes of the samples without any kind of compensation are represented

For each detection, the amplitudes of the post-compression samples of the eight pulses for the radar cell where the detection occurred (the one associated with the distance of the object) are represented.

These eight amplitudes of each detection are represented by red dots joined by lines. Also for each detection, the amplitude associated with the average power of these

eight pulses is represented by a black dot.

The applied detection threshold is represented by a green line.

All the black dots are above the green line because they represents the value that is compared to the threshold in order to decide that there is detection.

A blue line represents the system noise power level estimated by the signal process of the radar itself.

As expected, it can be observed that passes with the highest average Pd are those in which the amplitudes are globally well above the threshold.

It is also seen that the threshold acquires similar values in all the passes. As this threshold is obtained using CFAR techniques based on cell-averaging, the low variation of the threshold indicates that the noise power has remained stable throughout the data collection time.

This is directly indicated as well by the little variation of the blue line throughout each pass and between passes.

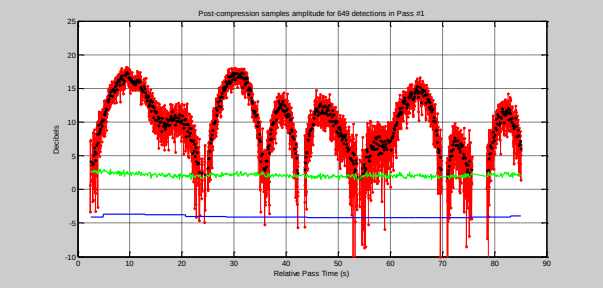

Figure 11. Raw post-compression samples for pass #1.

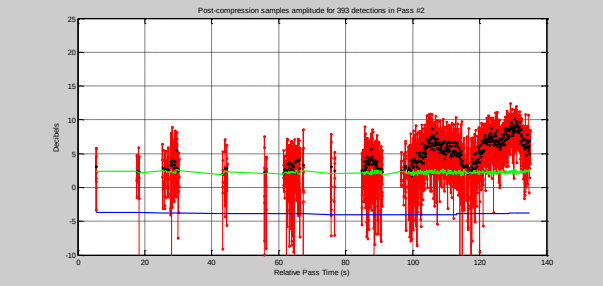

Figure 12. Raw post-compression samples for pass #2.

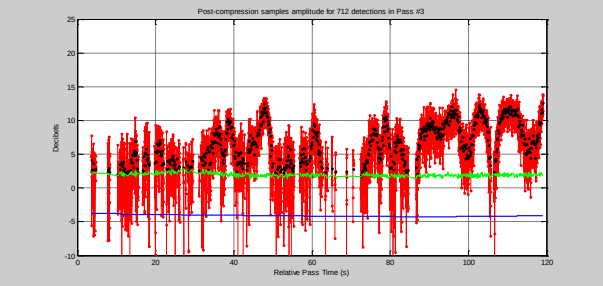

Figure 13. Raw post-compression samples for pass #3.

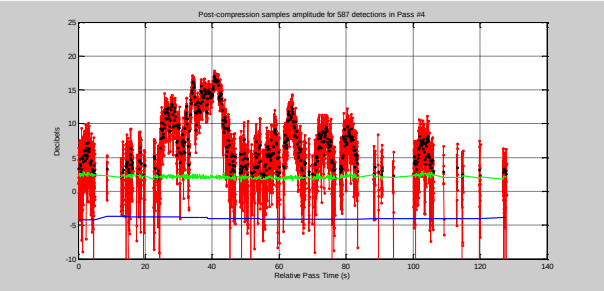

Figure 14. Raw post-compression samples for pass #4.

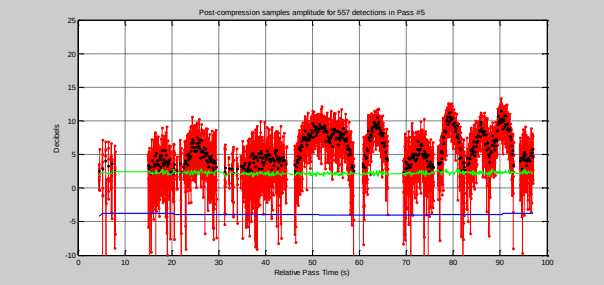

Figure 15. Raw post-compression samples for pass #5.

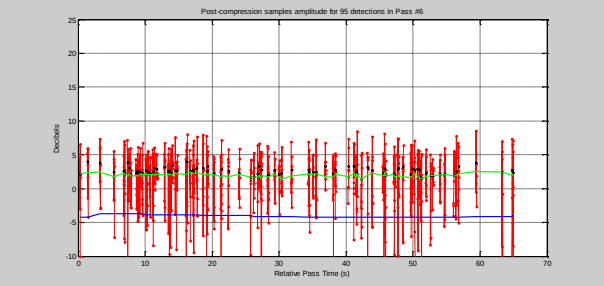

Figure 16. Raw post-compression samples for pass #6.

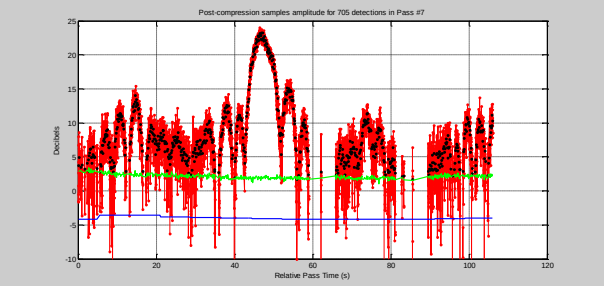

Figure 17. Raw post-compression samples for pass #7.

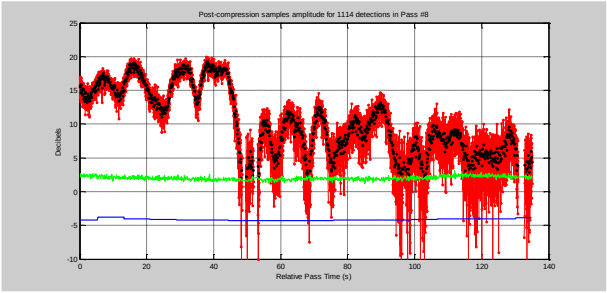

Figure 18. Raw post-compression samples for pass #8.

The most significant detail in the previous curves are the modulations that have the amplitude throughout each pass. It is manifested both, in the variation of the average detection amplitude and in the pulse-to-pulse variation itself.

To illustrate the pulse-to-pulse amplitude variation, the following figure zooms in on the highest-level region for Pass #7, allowing seeing the amplitudes of the eight pulses for detections offering S/N ratios between 25 and 27 dB.

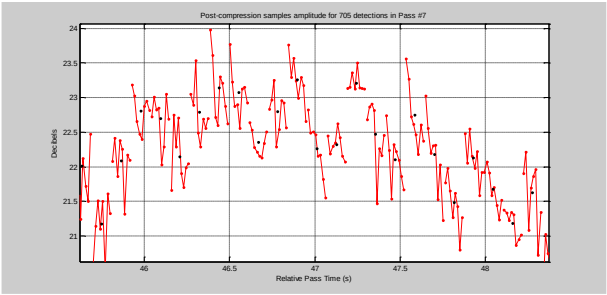

Figure 19. Raw post-compression samples for pass #7 (zoom).

In principle, this pulse-to-pulse S/N variation could be due to the influence of noise.

To assess whether this is the case, the following exercise is carried out:

• A matrix of eight rows and n columns is generated, where n is a very large number (for example, 10000) of complex Gaussian random variables of unit power, and a signal component of power S is added to it. They will therefore be simulated samples of the target signal S/N = S.

• For the eight samples of each column, the ratio in dB between the sample with the highest amplitude and the one with the lowest amplitude is calculated, and the values obtained for the n columns are averaged.

• The above is repeated for various values of S, thus obtaining the variation versus S/N of the mean.

Results of this simple statistical simulation process are shown in the following figure. It can be seen that, for example, for S/N = 26 dB, the average value of the amplitude dispersion in the 8 pulses would be about 0.9 dB. Looking again at the previous figure, it is seen that the detections whose average amplitude is around 22 dB, which corresponds to an S/N of approximately 26 dB, have dispersions that are not much greater than 1 dB.

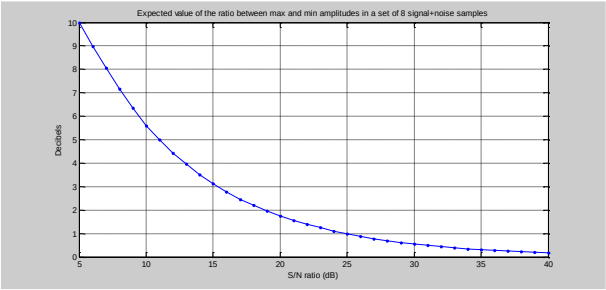

Figure 20. Expected max to min ratio of amplitude in eight pulses.

Since there are no captures with a very high S/N value, for now it is assumed that the pulse-to-pulse amplitude variations are simply a consequence of the uncorrelation of the noise and the low S/N ratio.

Therefore, attention should be focused on the modulation of the average amplitude of the signal reflected by the target, which in some cases is so strong that it causes detection loss intervals in passes where the object provides an high overall average Pd (for example, pass #7).

The next section introduces corrections to these amplitude values. These are applied to the mean amplitude to compensate for variations due to radar distance, beamshape, deflection and compression losses.

Specifically, the following is done:

- The estimated noise power is subtracted from the average power of the samples of the eight pulses so that an estimate of the power of the signal remains.
- Distance losses are compensated by adding the term $40 \cdot \log_{10} \frac{R}{R_{ref}}$, where R is the detection distance and Rref is an arbitrary distance set to 1000 km.
- Beamshape losses are compensated by adding the losses in dB for both the Tx beam and the Rx beam that originates the detection.
- Deflection losses are compensated by adding the losses in dB calculated with the simplified model.

- Compression losses are compensated by adding the level reduction associated with the shape of the compressed pulse, taking into account the position of the object relative to the radar cell.

These corrections do not take into account the small variations in the propagation losses due to distance, since for all the distances considered the object is outside the atmosphere.

The signal level remaining after these corrections should be proportional only to the radar cross section of the object (but it does not represent directly the RCS in dBm^2). The values obtained are shown in the following eight figures.

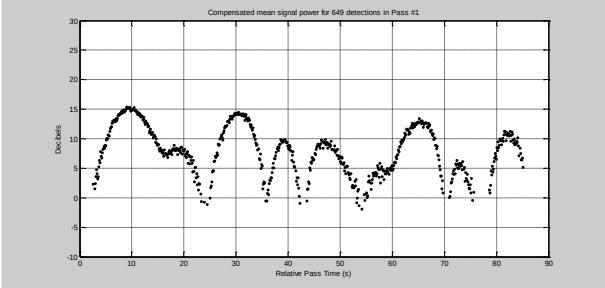

Figure 21. Corrected average power for pass #1.

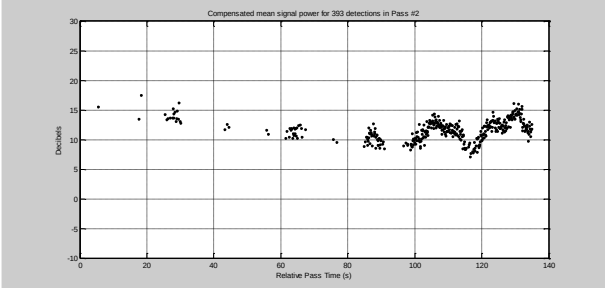

Figure 22. Corrected average power for pass #2.

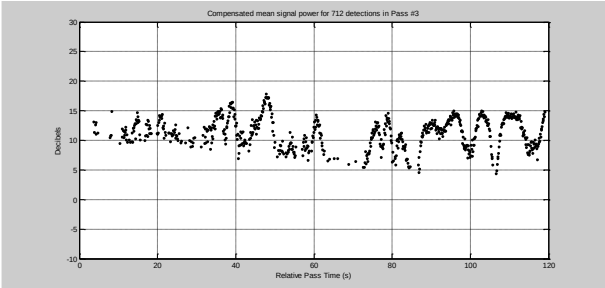

Figure 23. Corrected average power for pass #3.

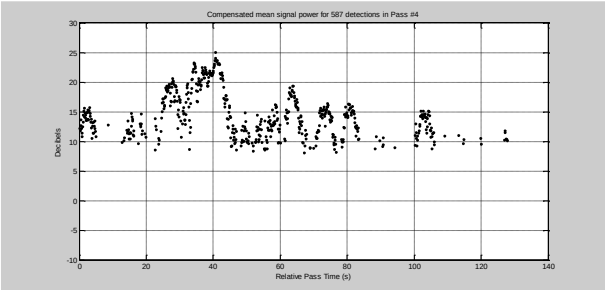

Figure 24. Corrected average power for pass #4.

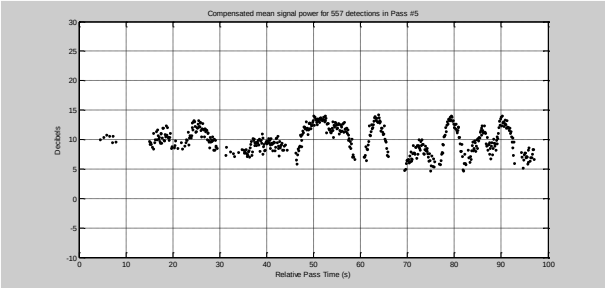

Figure 25. Corrected average power for pass #5.

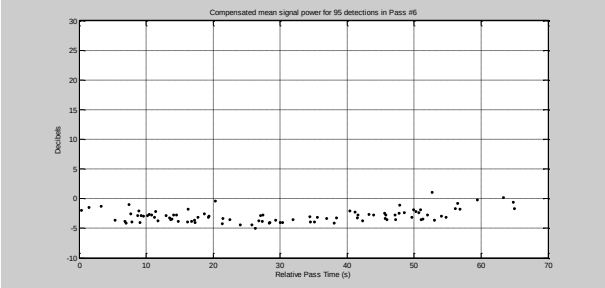

Figure 26. Corrected average power for pass #6.

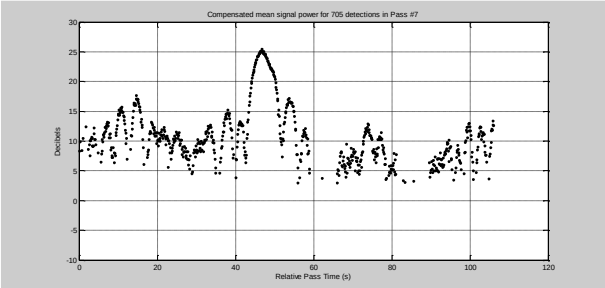

Figure 27. Corrected average power for pass #7.

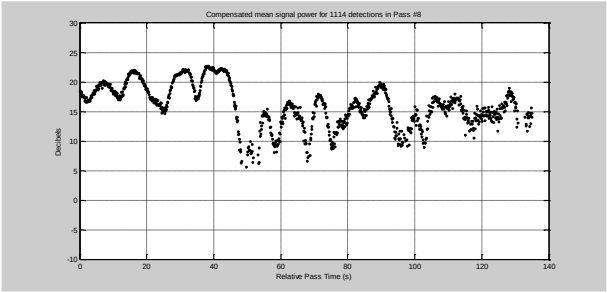

Figure 28. Corrected average power for pass #8.

What would be expected with respect to the previous curves would be almost constant values, with fluctuations only due to the influence of noise. However, it can be observed that although there is a greater degree of flattening with respect to the raw amplitudes, the significant modulations of the amplitude are still clearly appreciated.

In principle, all following causes could explain these modulations:

- The real deflection losses of the Rx antenna are clearly different from those assumed in the simple model considered in the compensation and present modulations as a function of pointing. In other tests carried out during the commissioning of the S3TSR radar it was seen that the variations in received power for the same satellite (once the losses due to beamshape and variation of the distance were compensated) fits quite well to the simplified model of deflection losses. These modulations such as those shown in the previous figures were not observed. Therefore, this cause is unlikely.

- The transmitted signal that bounces in the object presents a level variation versus time that is observed in the curves. This could be because:

    - Variations in the output power of the High Power Amplifiers (HPAs) that provide signal to the elements of the Tx antenna: It is ruled out because this would be associated with BITE reports that do not occur.

    - Problems in the beamforming of the Tx that causes the object not to be always "illuminated" with maximum gain: This is considered very unlikely because due to the way the aiming of the beams is controlled, abrupt changes in speed would be observed every 34 illuminations of the target (3.9 sec). Furthermore, taking into account the estimated RCS for the DANDE object (pass #6), if the Tx pointing had not been correct, its occasional detection would have been impossible.

    - The real deflection losses of the Tx antenna are clearly different from those assumed in the simple model considered in the compensation and level modulations are a function of pointing: If this had occurred, the active impedance of the antenna would have generated reports of BITE associated with high reflected power, and these reports have not occurred.

- Modulations are produced by multipath effect. This effect typically causes lobing in the received signal. The vertical reflection in the surrounding terrain is most of the times the most frequent cause of multipath.
  Since the terrain close to the radar antennas is basically flat, it can be assumed that the reflected component would arrive at the radar with an elevation angle equal to that of the direct component, but with a negative sign.
  The first of the following figures shows the elevation angle of the direct component for the eight passes.
  In the second figure, the deflection angle of this direct component is calculated, which is the angle formed by the direction vector towards the object with the normal to the antenna. As expected, this angle will be less than 90°, since the passes correspond to intervals in which the objects are in the visible hemispheres for the antennas.
  The third figure shows the deflection angle calculated for the case of the reflected signal, that is, the one that would arrive from the same azimuth, but with negative elevation. It can be seen that in all cases, the angle is greater than 90°, that is, it corresponds to the hemisphere not visible to the antenna.
  Therefore, these signals reflected on the ground would be received with a very large attenuation. In short, the geometric orientation of the Tx and Rx antennas, both with a nominal tilt of 60°, together with the range of elevations explored makes it very difficult for a significant multipath effect to occur.

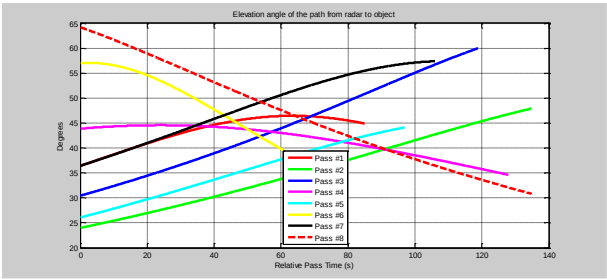

Figure 29. Elevation angle radar-object.

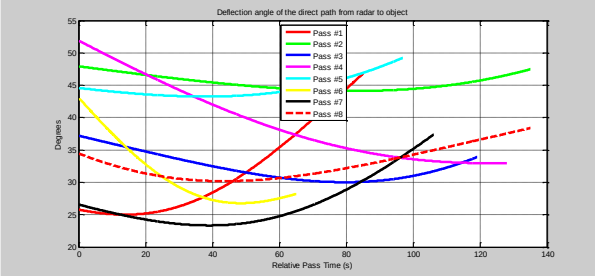

Figure 30. Deflection angle direct path.

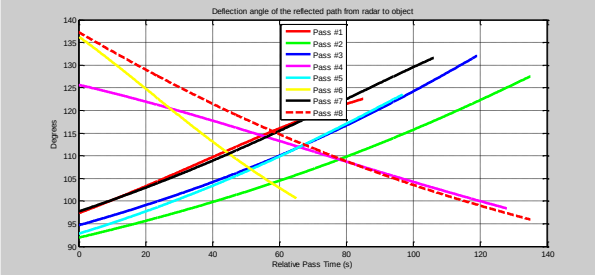

Figure 31. Deflection angle reflected path.

- Temporal variation in the Radar Cross Section of the object due to the combination of having a complex shape and its aspect ratio changing throughout the pass.
  This last explanation seems undoubtedly the most plausible.
  It is supported by the fact that, although few detections have been obtained for the only object that is supposedly spherical (pass #6), and the S/N ratio is very low for them, it is the only case in which modulations are not appreciated.
  The aspect ratio of the object will change due to two reasons:

    - The translation movement itself through the orbit.

    - Spinning (or tumbling) movements of the object with respect to the orbit-based reference system.

  To analyze the first point, we first define the orbit-based Cartesian reference system. The unit vectors that define it would be:

    - $\hat{y}$ (along-track): In the direction of the velocity vector.

    - $\hat{z}$ (cross-track): In the direction normal to the orbit plane. It is obtained by normalizing to unit module the vector product of the position vector centered on the ground and the velocity vector.

    - $\hat{x}$ (radial): It is obtained as the vector product $\hat{y} \times \hat{z}$.

  View angles α, β and γ are defined as those formed between the direction vector that goes from the object position to the radar position, and the three previous unit vectors $\hat{x}$, $\hat{y}$ and $\hat{z}$, respectively.
  The following figures show how these three angles vary throughout the eight passes. These variations would give us an idea of the rate of change of the aspect ratio, without taking into account the spinning movement of the object itself.
  The following table summarizes the variations that the three angles have (maximum minus minimum value), and as a summary value, the sum of these three variations:

Table 6. View angles.

Pass #	NoradId	Name	Δα	Δβ	Δγ	Δ
1	20666	SL-6 R/B(2)	8.9°	42.7°	5.7°	57.3°
2	15483	SL-8 R/B	17.9°	31.6°	13.5°	63.0°
3	25400	SL-16 R/B	23.5°	32.1°	6.1°	61.7°
4	23087	COSMOS 2278	7.6°	37.0°	4.9°	49.4°
5	22286	COSMOS 2228	14.0°	31.7°	14.0°	59.8°
6	39267	DANDE	14.5°	40.4°	4.8°	59.8°
7	00733	THOR AGENA D R/B	17.2°	36.6°	9.5°	63.3°
8	24298	SL-16 R/B	26.7°	34.3°	8.3°	69.2°

As can be seen, in all passes there are significant changes in these angles, being β the one that varies the most (the angle between the line of sight and the velocity vector). This angular variation, combined with the fact that the objects have complex shapes, could be enough to explain the recorded level variations.

However, if the spinning movement of the object were taken into account, that is, if the angles were recalculated with respect to a reference system centered and oriented on the object, the variations would be much greater, especially for uncontrolled objects.

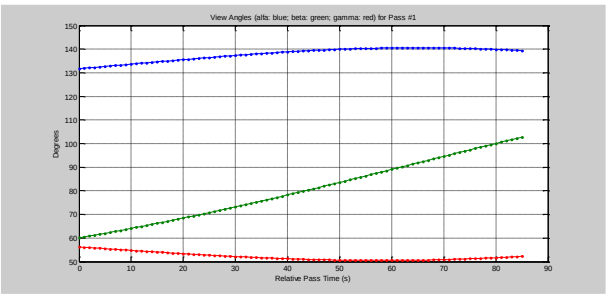

Figure 32. View angles for pass #1.

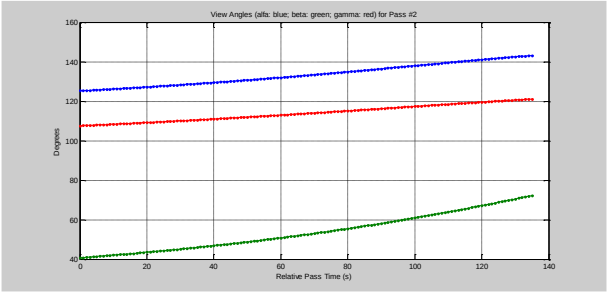

Figure 33. View angles for pass #2.

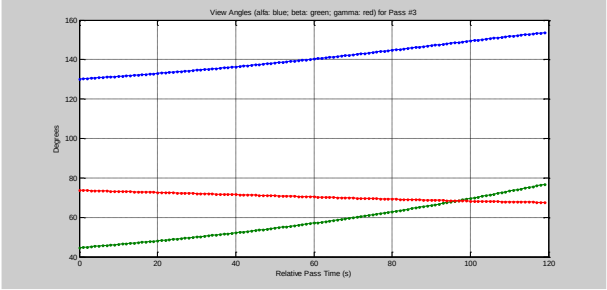

Figure 34. View angles for pass #3.

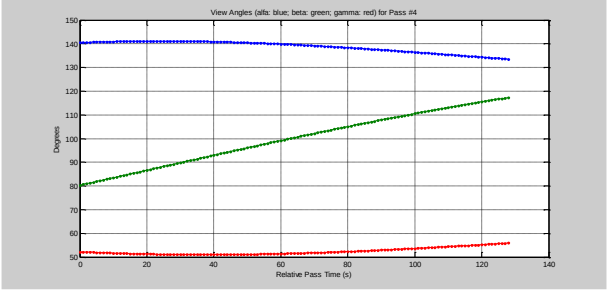

Figure 35. View angles for pass #4.

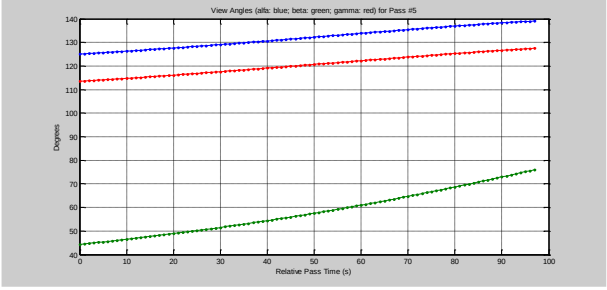

Figure 36. View angles for pass #5.

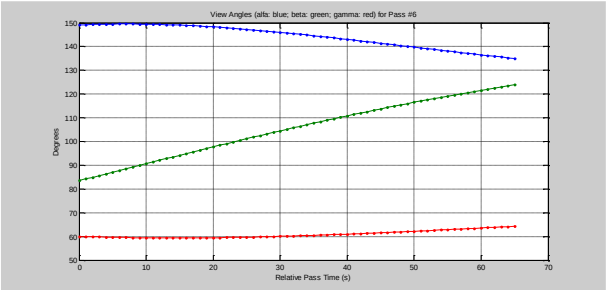

Figure 37. View angles for pass #6.

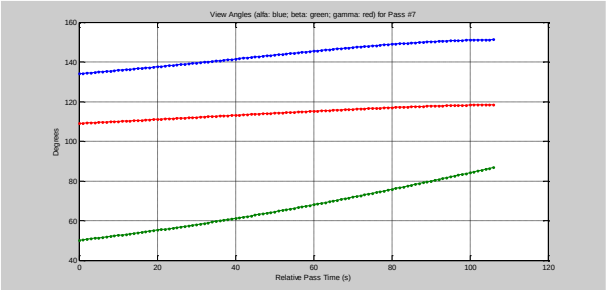

Figure 38. View angles for pass #7.

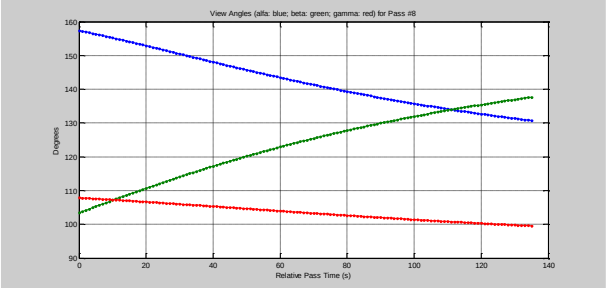

Figure 39. View angles for pass #8.

7 ANALYSIS OF SIGNAL PHASE

The S3TSR radar currently applies a Non-Coherent Integration (NCI) process in the normal surveillance operational mode.

However, it is a full coherent radar that could exploit the estimated signal phase variation to perform the typical processes on complex signals, based on FFT or similar, which theoretically require a lower S/N ratio than NCI to achieve the same Pd.

The previous analysis of amplitudes suggests that variations in the instantaneous RCS of the object occur throughout the pass, and that this causes the observed amplitude variations.

A question arisen is whether it is also possible to extract

from the signal phase variations that can also be attributed to the variation of the instantaneous RCS.

In the following, the variations with time of the relative phases of the received pulses will be analyzed in detail:

- We will use the subscript 0 to refer to instants in which pulses are emitted leaving the radar, the subscript 1 for instants in which the signal reaches the object and is reflected by it, and the subscript 2 for instants in which the reflected signal reaches back the radar. Let us assume that the reflection process is instantaneous.

- We will use the superscript S to refer to instants relative to the beginning of the emitted pulse, and the superscript E for instants relative to the end of the pulse.

- Consider a set of N consecutive radar pulses. Let us call $t_0^S[i]$ the instant at which the i-th transmitted pulse begins to be emitted from the radar, with i = 0, 1,…, N-1, where N is the number of pulses in the train of pulses to be processed as a block:

$$t_0^S[i] = t_0^S[0] + i\,T \qquad (1)$$

$$t_0^E[i] = t_0^S[i] + \tau[i] \qquad (2)$$

Where T is the duration of the interpulse period (14.35 ms) and where τ[i] is the duration of the ith pulse (around 1 ms).

- On the other hand, let $\boldsymbol{\rho}(t)$ be the function that provides the position vector in Cartesian coordinates as a function of time with respect to an inertial system (ECI), and let $\mathbf{s}(t)$ be the function that provides the radar position vector with respect to that same inertial frame.

- Let's assume for now propagation in free space, and more specifically, in vacuum. The instant $t_1^S[i]$ in which the beginning of the pulse will reach the object must comply:

$$c\,(t_1^S[i] - t_0^S[i]) = \| \boldsymbol{\rho}(t_1^S[i]) - \mathbf{s}(t_0^S[i]) \| \qquad (3)$$

  Where $\| v \|$ represents the norm 2 of the vector v, that is, its magnitude, and c is the speed of light.
  In the same way, the instant $t_1^E[i]$ in which the end of the pulse will reach the object will be the one in which:

$$c\,(t_1^E[i] - t_0^E[i]) = \| \boldsymbol{\rho}(t_1^E[i]) - \mathbf{s}(t_0^E[i]) \| \qquad (4)$$

- In the same way, the instants $t_2^S[i]$ and $t_2^{SE}[i]$ in which the beginning and end of the reflected pulse are received by the radar will be those that satisfy:

$$c\,(t_2^S[i] - t_1^S[i]) = \| \mathbf{s}(t_2^S[i]) - \boldsymbol{\rho}(t_1^S[i]) \| \qquad (5)$$

$$c\,(t_2^E[i] - t_1^E[i]) = \| \mathbf{s}(t_2^E[i]) - \boldsymbol{\rho}(t_1^E[i]) \| \qquad (6)$$

  The duration of the received pulse τ'[i] will be given by:

$$\tau'[i] = t_2^E[i] - t_2^S[i] \qquad (7)$$

  And it will happen that in general τ'[i] is different from τ[i]. In fact, the modulation of the received signal will be different from that of the emitted signal since the time undergoes a scaling that in practice could be considered constant and equal to τ'[i]/τ[i].
  This scaling in time, applied to the case of linear phase variation, is what originates the Doppler shift.

- The delay on the reception of the beginning of the pulse and the distance-delay that would be derived from it, would be given by:

$$\Delta t_R[i] = t_2^S[i] - t_0^S[i] \qquad (8)$$

$$r[i] = (c/2)\,\Delta t_R[i] \qquad (9)$$

- Let us suppose that the reflection on the object produces a phase shift of the reflected signal with respect to the incident one that can be considered the same for the N pulses. We therefore assume that the phase variations observed in the N pulses are not due to changes in the phase of the reflection coefficient.

- Let us assume that the signal generation and reception processes are implemented in such a way that the N pulses are emitted with the same initial phase, which we are going to assume is 0, and that at the instant generation begins the phase of the numerical oscillator associated with reception and demodulation is also set to 0. Since this last oscillator "is as if it were acting" at the carrier frequency f_0, and since the reflected pulse is received with the same phase as the emitted pulse, it will happen that the initial phase of the ith received pulse $\Phi^S[i]$ will be given by the phase increment of the numerical

oscillator during the time elapsed between the emission and reception of the pulse:

$$\Phi^S[i] = -2\,\pi\,f_0\,\Delta t_R[i] \qquad (10)$$

- Apart from the absolute phase of the pulses, what we are interested in are the phase variations that are recorded from one pulse to another:

$$\Delta\Phi^S[i+1,i] = \Phi^S[i+1] - \Phi^S[i] = -2\,\pi\,f_0\,(\Delta t_R[i+1] - \Delta t_R[i]) = -2\,\pi\,f_0\,(2/c)\,(r[i+1] - r[i]) \qquad (11)$$

- Radar signal processing does not directly measure the phases of the pulse as it is received, but instead applies a compression process (matched filter) that concentrates the pulse energy, distributed over multiple samples into a single output sample per pulse.
  To avoid Doppler mismatch, the S3TSR uses LFM (chirp) waveforms. Although with this modulation a significant loss of compression gain is avoided when the received signal is affected by Doppler, it presents the drawback of the so-called range/Doppler coupling.
  It consists in the fact that the compression peak appears really changed in distance by an offset equal to the product of the average radial velocity that affects the pulse ($v_r[i]$), and a parameter of temporal offset associated with the pulse ($\Delta w[i]$) that it only depends on its characteristics and the carrier frequency. Specifically, calling $r_C[i]$ the distance derived from the estimation of the position of the post-compression peak for pulse i, we have:

$$r_C[i] = r[i] + v_r[i]\,\Delta w[i] \qquad (12)$$

  with:

$$\Delta w[i] = f_0\,\tau[i] / B \qquad (13)$$

  Where B is the bandwidth (frequency excursion) of the pulse, but affected by the sign of the LFM slope. For example, for positive slope and negative radial velocity (the target is approaching), the distance associated with the post-compression peak will be less than the actual distance to the target.

- On the other hand, the phase of the post-compression peak sample ($\Phi_C[i]$) will depend on the initial phase of the received pulse, plus a contribution due to the average Doppler frequency affecting the pulse. Specifically:

$$\Phi_C[i] \approx \Phi^S[i] + 2\,\pi\,f_D\,(\tau[i]/2) = \Phi^S[i] - 2\,\pi\,f_0\,v_r[i]\,\tau[i] / c \qquad (14)$$

- And the pulse-to-pulse variations measured in the compression peak phase would be given by:

$$\Delta\Phi_C[i+1,i] = \Phi_C[i+1] - \Phi_C[i] = \Delta\Phi^S[i+1,i] - 2\,\pi\,f_0\,(v_r[i+1]\,\tau[i+1] - v_r[i]\,\tau[i]) / c \qquad (15)$$

  That is:

$$\Delta\Phi_C[i+1,i] = -2\,\pi\,f_0\,\Delta t_C[i+1,i] \qquad (16)$$

  with:

$$\Delta t_C[i+1,i] = (2/c)\,[\,r[i+1] - r[i] + 0.5\,(v_r[i+1]\,\tau[i+1] - v_r[i]\,\tau[i])\,] \qquad (17)$$

In summary, in case there are no variations in the phase of the radar section or in the insertion phases of the Tx and Rx paths, there must exist a relationship, given by the previous expression, between the pulse-to-pulse phase variations. that are conveyed by the compressed signal, and the pulse-to-pulse variations that are found in the distance-delay r[i] and its derivative velocity $v_r[i]$.

The analysis that is done to find out if this is valid in practice is detailed in the following bullets:

- It is considered a set of detections that have a relatively high S/N ratio and correspond to a one-pass interval where clear amplitude modulation is observed. Specifically, an interval of about 7s is selected in the central part of Pass #7.
  It is a set of 62 detections, which in total are 496 pulses. The figure below shows the post-compression peak sample amplitude for these 496 pulses.

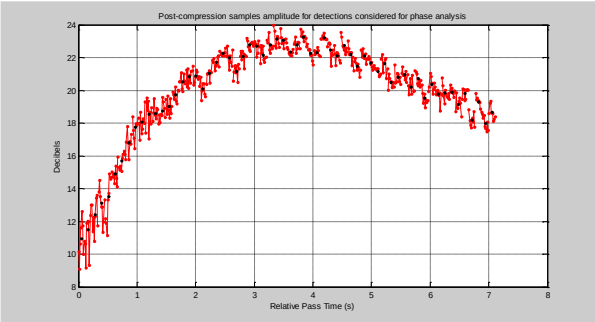

Figure 40. Post compression samples (zoom) for Pass #7.

- Starting from the 62 distances associated with the detections, which correspond to post-compression estimates, the delay-distances associated with each of the pulses are obtained.
  It is done with an iterative process with degree 4 polynomial fits. It starts with a polynomial that fits the distribution of post-compression distances. Deriving the polynomial, the one associated with the radial velocity is obtained. With the already estimated radial velocity, the distance offset ($v_r[i]\,\Delta w[i]$) is calculated, which must be subtracted from the post-compression distance to obtain the delay distance.
  Next, another polynomial is calculated, but one that is now adjusted to the distance-delays, obtaining a new radial velocity estimate that allows refining the distance offset, which is applied again to the post-compression distances to obtain a new estimate of the distances-delay. This previous process is repeated until convergence is obtained.
  The first of the following figures shows the starting post-compression distances (black x's), the first fit polynomial (red line) and the finally estimated delay-distances for each pulse.

  The second figure shows the estimated radial velocity for each of the pulses.

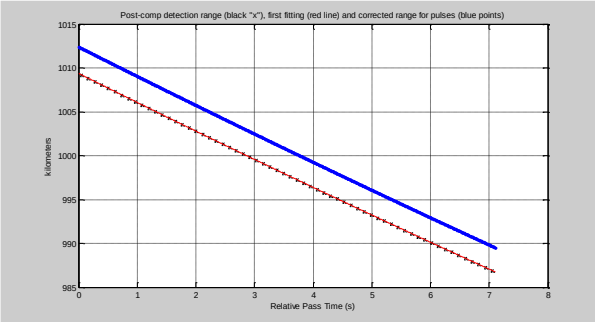

Figure 41. Post compression distances.

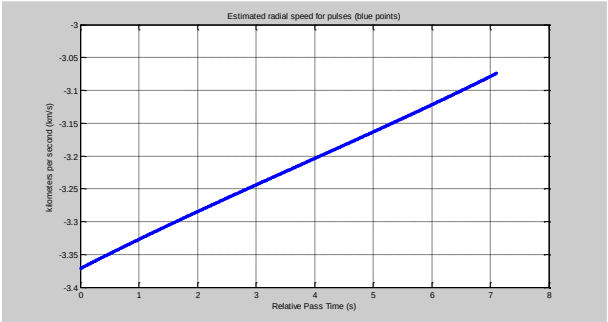

Figure 42. Estimated radial speed.

- Once the distances and speeds are calculated, it is possible to calculate the values of $\Delta t_C[i+1,i]$, and multiplying by $-2\pi f_0$, we would obtain the expected phase variations, which will be compared with the phase variations of the post-compression samples.
  However, given the high radial velocity, and the relatively high interpulse period, variations are on the order of hundreds of thousands of degrees.
  Since the phase difference for the post-compression samples will be ±180°,it is necessary to apply a process to resolve the phase ambiguity.

- Therefore, the detection with the highest average level is considered, the 34th.
  For this detection, the value $\Delta t_C[i+1,i]$ that corresponds with the difference between the second and the first pulse is -0.3073 μs, but although it seems small, multiplying it by $-2\pi f_0$ leaves us with a phase variation of 153840°.
  On the other hand, the corresponding phase difference based on post-compression samples is 117.6°, so it is necessary to add $427427\times(2\pi)$ to obtain a result of 153837.6°, a value that is already comparable and very close to the expected.
  Since the second order phase variations, which are due to radial acceleration, are relatively small (around -30°), once the difference has been corrected for the first pair of detection 34th, to correct the rest it will suffice to apply the unwrap function to the successive phase differences. This process has to be done both, in increasing time until the last pulse of the last detection, and in decreasing time until the first pulse of the first detection.

- After applying the above process, the phase difference values shown in the following figure are obtained. To make the values easier to read, they are represented with the reference value of 153840° already substracted.

  It can be seen in the figure that they coincide quite a lot both in values and in slope in the central part, but when we move away from the center, systematic

divergences begin to be appear.

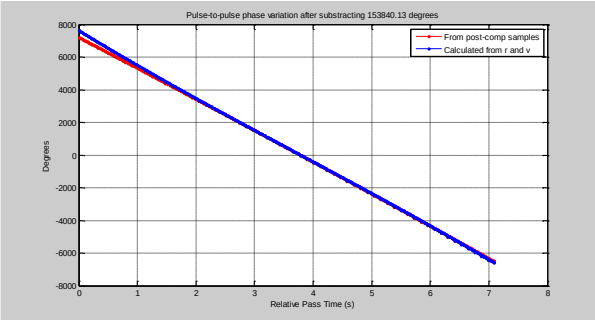

Figure 43. pulse-to-pulse phase variations (corrected).

To better observe difference in values, they are shown directly in the following figure. It can be seen how in the central part there is almost coincidence between the measured values and those calculated with r and v. However, gradually there are observable differences in the phase deltas, especially left on the central zone.

Comparing this figure with the one that showed the amplitudes of the samples, a clear correlation can be seen between changes in amplitude and changes in the phase slopes.

This reinforces the idea that it may be the aspect ratio change of the object, especially due to its spinning movement, which not only causes changes in the module of the radar section but also in its phase.

Small peaks that occur exactly every 8 pulses can also be seen in the figure.

It corresponds to the phase difference that is calculated between the first pulse of a detection (that is, from a new beam) and the eighth pulse of the previous detection (generated by the previous beam).

It is possible that in these cases there is a relatively large variation in the length of the pulses, and that there is some additional term in the estimation of the phase of the post-compression peak sample.

It may also happen that it is an effect associated with the beamforming, as the two beams have different pointing.

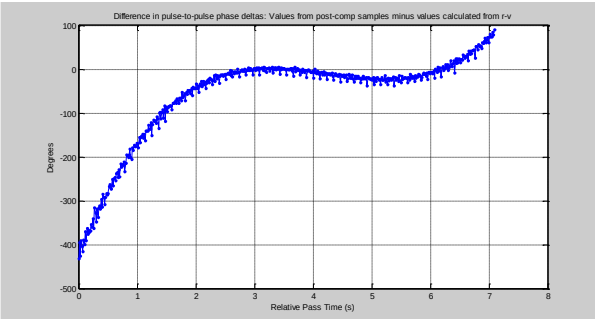

Figure 44. Difference in pulse-to-pulse phase variations.

In addition to the aforementioned correlation between amplitude variations and differences in phase deltas, another conclusion obtained from this analysis is that the S3TSR is effectively coherent in phase, so detection processes based on coherent integration could be implemented.

Phase "linearity" is best appreciated in the figure below, which shows a zoom of the previous figure.

It can be seen how the 7 phase differences obtained for the 8 pulses of a beam are well adjusted with respect to the line associated with radial acceleration.

It is evident that the detection process cannot be based on a simple FFT, since this is effective only in case the 7 phase variations coincide, that is, for zero or negligible radial acceleration.

Therefore, it is necessary either to a-priori know the radial acceleration of the object to be detected, or to propose multiple hypotheses.

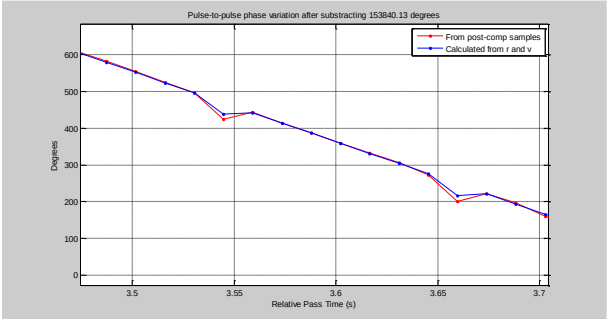

Figure 45. Difference in pulse-to-pulse phase variations (zoom).

8 CONCLUSIONS AND FUTURE WORK

As a most notable conclusion, it has been shown that, although the S3TSR is a system that, by specification, is currently permanently operating in Surveillance mode, it is possible, through configuration and special control, to follow specific space objects passing across its FoR.

In this experimental mode, the points of the successive beams are pointed towards the predicted position of the selected orbital object.

The number of plots generated for each object increases considerably compared to the one that is operating in Surveillance mode, which allows greater precision in the estimation of the orbit.

Additionally, the operation in this experimental mode has been combined with a special recording of detections,

which provides low-level data that is not available in the plot recordings normally supported by the system.

These special recordings contain the complex post-compression samples of the different channels for the radar cell associated with the detection.

The combination of both capabilities using a special control SW developed ad hoc, has been used to carry out a measurement campaign on December 22, 2022.

In this campaign, detections were recorded for eight object passes that have been discussed in this article.

The analysis of the amplitudes of the post-compression samples of the detections clearly shows amplitude modulations.

It was shown that the most likely reason for these modulations is variations in the radar cross section caused by the combination of a complex shape and the change in the aspect ratio of the object throughout the pass.

The analysis of pulse-to-pulse phase variations shows deviations from the expected values derived from the evolution of distance and radial velocity, which correlate with the modulations observed in amplitude.

Additionally, this analysis makes it possible to ensure that it would be possible to implement in the S3TSR alternative detection processes making use of coherent integration.

The intention is to repeat this type of testing and analysis in the future to further strengthen the conclusions.

It will be especially interesting to capture detections of supposedly spherical objects in passes with higher S/N ratio, and to capture the same object in several passes to correlate the amplitude modulations.

9 ACKNOWLEDGEMENTS

The authors would like to thank COVE (Centro de Operaciones de Vigilancia Espacial / Space Surveillance Operation Centre, from the Spanish Air and Space Force) for their full support during the test campaign carried out in the last days of December 2022.

10 REFERENCES

1. Gomez, R., Salmerón, J. M. V., Besso, P., Alessandrini, M., Pinna, G. M., & Prada, M. A. R. (2019, January). Initial Operations of the Breakthrough Spanish Space Surveillance and Tracking Radar (S3TSR) in the European Context. In *1st ESA NEO and Debris Detection Conference. Presented paper. Darmstadt, Germany*.